Scientific Reports

https://doi.org/10.1038/s41598-026-42993-z

Article in Press

Immunotolerant Oligomer scaffolds promote regenerative remodeling and improved muscle structure and function after volumetric muscle loss

Received: 10 November 2025

Accepted: 28 February 2026

Published online: 08 March 2026

Cite this article as: Morrison R.A., Sexton J., Zhang L. *et al.* Immunotolerant Oligomer scaffolds promote regenerative remodeling and improved muscle structure and function after volumetric muscle loss. *Sci Rep* (2026). https://doi.org/10.1038/s41598-026-42993-z

Rachel A. Morrison, Joshua Sexton, Lujuan Zhang, Eric Dong, Makayla Phillips, Hongyu Gao, Yunlong Liu, Taimoor H. Qazi, Stacey Halum & Sherry L. Voytik-Harbin

Immunotolerant Oligomer Scaffolds Promote Regenerative Remodeling and Improved Muscle Structure and Function After Volumetric Muscle Loss

Rachel A. Morrison[1†], Joshua Sexton[1†], Lujuan Zhang[2], Eric Dong[1], Makayla Phillips[1], Hongyu Gao[3], Yunlong Liu[3], Taimoor H. Qazi[1], Stacey Halum[2], Sherry L. Voytik-Harbin[1,4*]

[1]Weldon School of Biomedical Engineering, Purdue University, West Lafayette, IN 47907, USA
[2]Department of Otolaryngology-Head and Neck Surgery, Indiana University School of Medicine, Indianapolis, IN 46202, USA
[3]Department of Medical and Molecular Genetics, Indiana University School of Medicine, Indianapolis, IN 46202, USA
[4]Department of Basic Medical Sciences, Purdue University, West Lafayette, IN 47907, USA

[†]These authors contributed equally

*Corresponding author: Sherry L. Voytik-Harbin, E-mail: harbins@purdue.edu

Abstract

Volumetric muscle loss (VML) overwhelms endogenous repair mechanisms, leading to defect contraction, fibrosis, and persistent aesthetic and functional deficits. Restorative biomaterials capable of re-establishing muscle structure and function represent promising strategies for treating severe injuries where conventional surgical repair is inadequate. Using a rat full-thickness VML model, we evaluated Oligomer, an engineered collagen polymeric biomaterial, in three prototype scaffold configurations that differed in application format and microstructure, with untreated defects serving as controls. Muscle structure, function, and tissue response were assessed longitudinally, including spatial transcriptomic profiling. Oligomer scaffolds supported regeneration of organized muscle architecture, including aligned myofibers, vascular networks, and integrated neurovascular structures. Higher-density scaffolds preserved defect geometry and yielded greater recovery of muscle mass and contractile function. Spatial transcriptomic analyses defined a regenerative remodeling mechanism distinct from reparative or constructive remodeling, characterized by an immunotolerant environment that enabled infiltration of diverse progenitor populations, including pro-regenerative mesenchymal cells, pericytes, satellite cells, and endothelial and neural stem cells. This cellular niche supported coordinated activation of myogenic, vascular, and neural pathways, recapitulating key aspects of developmental myogenesis. Collectively, these findings establish the mechanistic foundation for Oligomer scaffold-mediated regenerative remodeling and demonstrate its potential as a restorative biomaterial for treatment of VML.

Keywords: type I oligomeric collagen, regenerative remodeling, restorative biomaterial, spatial transcriptomics, volumetric muscle loss, skeletal muscle

Introduction

Volumetric muscle loss (VML) is a devastating clinical condition that occurs when large portions of skeletal muscle are irreversibly lost due to trauma, tumor resection, or combat-related injuries. Affected individuals often experience disfigurement, profound weakness, reduced mobility, chronic pain, and loss of independence, frequently requiring assistive devices or caregiver support. Current standards of care rely on surgical approaches such as autologous tissue flaps or free functional muscle transfers[1–3]. Although these procedures can provide wound coverage or partial restoration of muscle volume, functional recovery, particularly in terms of strength, endurance, and range of motion, remains limited[1,3,4]. Moreover, these interventions are constrained by donor-site morbidity, technical complexity, and risk of long-term complications, including graft atrophy and flap failure[2,5]. Off-the-shelf biomaterial approaches, such as decellularized extracellular matrix (dECM) scaffolds, have been evaluated in preclinical and clinical settings; however, their immune-mediated degradation (bioresorption) typically results in fibrotic connective tissue formation rather than regeneration of functional muscle[6,7]. Thus, there remains a critical unmet need for regenerative therapies that not only restore muscle volume, architecture, and mechanical continuity but also integrate with host tissue to support adaptation, remodeling, and long-term functional recovery[8].

Skeletal muscle is a highly organized tissue whose hierarchical architecture underlies its physiological function. At the molecular level, actin and myosin filaments assemble into sarcomeres, the fundamental contractile units that align in series to form myofibrils. These myofibrils are bundled into multinucleated myofibers, which are further organized into fascicles surrounded by connective tissue sheaths that house resident blood vessels, nerves, and satellite and immune cells (**Supplementary Figure S1**). This multiscale architecture sustains the high metabolic demands of muscle and enables both longitudinal and lateral force transmission, supporting coordinated contraction, efficient load transfer, and functional movement[9,10]. Importantly, skeletal muscle is among the most regenerative tissues in the body. Following small-scale injuries such as exercise-induced microtrauma, contusions, or minor lacerations, resident satellite cells activate, proliferate, and fuse to repair damaged fibers, typically restoring both structure and function[11,12]. In contrast, loss of large volumes of muscle tissue, as in VML, creates significant dead space and disrupts the ECM scaffold and its integrated neurovascular networks, leading to a loss of the structural and mechanical continuity required for coordinated muscle regeneration and force transmission. This disruption shifts the healing response from regeneration to reparative fibrosis, resulting in persistent void contraction, impaired signaling, and diminished functional recovery[13]. Reparative healing is further characterized by reduced satellite cell migration, recruitment of macrophages and fibroblasts, and

deposition of avascular, disorganized fibrous tissue that replaces functional muscle[6].

Over the past decade, extensive efforts have focused on developing regenerative and restorative strategies for skeletal muscle, as summarized in several recent comprehensive reviews[5–7,14–16]. These efforts can be broadly classified into three categories: i) implantable biomaterials; ii) combinatorial materials incorporating cells and/or bioactive factors (including 3D bioprinting approaches); and iii) ex vivo engineering of skeletal muscle replacements. Interest in dECM materials remains strong, with studies evaluating autologous, allogeneic, and xenogeneic sources derived from dermis, adipose tissue, pericardium, urinary bladder (UBM), skeletal muscle, and small intestinal submucosa (SIS). Although these scaffolds retain key aspects of native ECM architecture and biochemical signaling, they continue to yield variable regenerative outcomes and incomplete functional recovery, with results highly dependent on tissue source and decellularization protocol employed[17,18]. Natural hydrogel systems, including those based on collagen, fibrin, hyaluronic acid, and alginate, have been evaluated for their injectability, cytocompatibility, and ability to support cellular remodeling. These materials are often enhanced through fabrication techniques such as electrospinning, microgrooving, or patterned assembly to promote myofiber alignment and anisotropy[19–21]. In parallel, biofabrication strategies employing three-dimensional (3D) bioprinting or modular assembly of myogenic and vascular cells within anisotropic scaffolds, frequently combined with electrical and/or mechanical stimulation, have demonstrated improved fiber alignment, vascularization, and partial innervation in small-animal models[22,23]. Emerging transcriptomic and single-cell profiling analyses are further elucidating molecular pathways governing myogenesis, angiogenesis, and immune modulation, providing valuable design cues for next-generation therapies[13,24–27]. Despite these advances, most strategies remain constrained by insufficient mechanical stability, limited nutrient diffusion, and challenges in reproducibility, scaling, and regulatory translation.

Ideal biomaterials for functional muscle restoration should be available in an off-the-shelf format compatible with surgical workflows, exhibit high biocompatibility to avoid inflammatory or foreign body responses, and provide biophysical and biochemical cues to guide progenitor cell migration, activation, and differentiation into organized, functional myofibers[6,14]. They should also promote vascularization and innervation to restore contractile function, while being amenable to scalable manufacturing and a straightforward regulatory pathway to clinical adoption[6,14]. Biomaterials that meet these combined biological, functional, and translational requirements are referred to here as “restorative biomaterials”, reflecting their capacity to re-establish tissue continuity, organized architecture, and functional integration rather than undergoing fibrotic scar formation. The Oligomer engineered collagen platform was developed to address these biological and translational needs. Polymerizable type I oligomeric collagen (Oligomer) represents a unique collagen protein building block that, under physiologic conditions, self-assembles through hydrophobic and electrostatic interactions to form mechanically stable scaffolds replicating the ultrastructure of native collagen fibrils[28–30]. Like synthetic polymers, this biopolymer can be formulated into a range of scaffold formats, from injectable in-situ polymerizing

scaffolds to preformed scaffolds with tunable fibrillar microstructural and mechanical properties[30,31]. Across multiple in vitro models[29,32–34] and preclinical models, including dermal regeneration[35], injection laryngoplasty[36], breast-conserving surgery[37], and laryngeal reconstruction involving muscosal, muscular, and cartilaginous replacements[38–40], these scaffolds have consistently been shown to support vasculogenic and myogenic cell behavior in vitro, as well as cellular infiltration, vascularization, and organized tissue restoration. A key differentiator of this platform is its regenerative mode of action in vivo. Unlike conventional materials that trigger inflammatory-mediated fibrotic capsule formation or degradation, Oligomer scaffolds persist after implantation, integrate with host tissue, and support immunotolerance and regenerative remodeling that restores both tissue form and function[41]. Importantly, this regenerative remodeling mechanism enables restoration of structural and mechanical continuity and supports long-term adaptation and growth with the host. Notably, an in-situ scaffold-forming formulation from this platform recently achieved FDA 510(k) clearance for wound management, underscoring its translational readiness.

In this study, we investigated the restorative potential of engineered collagen polymeric Oligomer scaffolds in a preclinical rat model of VML. As summarized in **Figure 1**, full-thickness defects encompassing ~30% of tibialis anterior (TA) muscle volume were created and treated with one of three Oligomer scaffold prototypes that differed in application format and fibrillar density: (1) an in-situ polymerizing injectable scaffold, (2) a low-density preformed scaffold, and (3) a high-density preformed scaffold. Untreated defects served as controls. This design enabled us to test the hypothesis that Oligomer scaffolds, by supporting immunotolerant regenerative remodeling rather than immune-mediated degradation and constructive remodeling, would promote restoration of muscle structure and function following volumetric muscle loss, and that differences in scaffold format and fibrillar density would modulate these outcomes. To comprehensively evaluate outcomes across scales, we integrated in-vivo muscle function testing, gross morphometric and histological analyses, and immunolabeling analyses, together with spatial transcriptomics to define the cellular and molecular programs of scaffold-guided remodeling. Collectively, this approach provides new mechanistic insight into how Oligomer scaffold design directs regenerative versus reparative (fibrotic) healing pathways in VML.

Methods

Oligomer Scaffold Preparation

Three prototype Oligomer scaffolds were fabricated from polymerizable type I oligomeric collagen (GeniPhys, Indianapolis, IN): (1) In-Situ Scaffold, a flowable, in-situ self-assembling scaffold formulation with a fibrillar density of ~7 mg/cm^3; (2) Low Density (LD) Scaffold, an implantable scaffold with a fibrillar density of ~20 mg/cm^3; and (3) High Density (HD) Scaffold, an implantable scaffold with a fibrillar density of ~50 mg/cm^3. Scaffold fibrillar density was defined as the mass of polymerized oligomeric collagen per unit scaffold volume (mg/cm^3). For the In-Situ Scaffold**,** an acidic Oligomer solution was mixed with a phosphate buffer-based self-assembly reagent and flowed into the VML defect, where it polymerized (self-assembled) into a scaffold in situ. Based on previous studies of in-situ self-assembling oligomeric formulations, the resultant scaffolds are expected to exhibit

a largely isotropic fibrillar microstructure upon formation within the tissue void[30,37]. For the LD and HD Scaffolds, an Oligomer solution was polymerized in a cylindrical mold (diameter: 3.4 cm) and subjected to compression densification with porous platens positioned on the top and bottom surfaces[30,31,42] to produce 4-mm thick scaffolds at the specified fibrillar densities. Previous studies have shown that fabrication of Oligomer scaffolds using this compression densification format yields an anisotropic microstructure with spatial gradients in fibril density and alignment parallel to the scaffold top and bottom surfaces. Specifically, these scaffolds exhibit higher densities of more highly aligned fibrils near the scaffold surfaces and lower densities of less aligned fibrils toward the scaffold interior[30,31,42]. Scaffolds were trimmed to the VML defect size using a 10 mm × 5 mm ellipsoidal biopsy punch (Integra, Mansfield, MA).

Rat VML Surgical Procedures and Animal Care

This study is reported in accordance with the ARRIVE guidelines. All animal procedures were conducted in accordance with AAALAC guidelines and approved by the Purdue University Institutional Animal Care and Use Committee (IACUC). An overview of the rat VML model, experimental groups, timeline, and outcome measures is provided in **Figure 1**. Male Lewis rats (~360 g; Inotiv, West Lafayette, IN) were used, with 4-6 animals per group at each time point (2, 8, and 16 weeks). Animals were randomly assigned to one of four treatment groups: (1) Oligomer In-Situ Scaffold, (2) Oligomer LD Scaffold, (3) Oligomer HD Scaffold, or (4) no treatment control (untreated defect).

Anesthesia, Analgesia, and Perioperative Care

For all animal survival procedures, including muscle defect creation, scaffold implantation, and muscle function testing, anesthesia was induced in an induction chamber and maintained using a nose cone attached to a rodent anesthesia manifold, with isoflurane delivered at 1.5–3% in oxygen. Animals were positioned on a thermal control unit to maintain body temperature. Following induction, veterinary ophthalmic ointment was applied to both eyes to prevent desiccation. Analgesia was provided prior to VML surgery using extended-release buprenorphine (Ethiqa XR, 0.65 mg/kg, subcutaneous; Fidelis Animal Health, North Brunswick, NJ) to minimize pain and distress after surgery.

At designated study endpoints, rats were anesthetized for muscle function testing as described for survival procedures. Analgesia was provided using buprenorphine (0.02 mg/kg, subcutaneous; Covetrus, Portland, ME) to minimize pain during surgery. After completion of study outcomes, animals were deeply anesthetized with 5% isoflurane and euthanized by intracardiac administration of an overdose of pentobarbital solution (>1 mL/10lb; Covetrus), in accordance with AVMA guidelines.

VML Surgery

Under anesthesia, the left hindlimb was shaved and disinfected. The fascia was bluntly dissected from the TA muscle, which was then separated from the underlying tibia and extensor digitorum longus (EDL). A full-thickness volumetric muscle defect (~30% of TA volume) was created using a 50 mm^2 ellipsoidal biopsy punch. The In-Situ Scaffold component solutions were mixed according to manufacturer instructions and applied to the defect, where it polymerized in situ.

The LD and HD Scaffolds were trimmed and press-fit into the defect. No treatment control animals received no implant. Fascia and skin were closed with 6-0 Vicryl absorbable sutures (Ethicon, Raritan, NJ).

Muscle Function Testing

TA muscle function was evaluated in individual animals using minimally invasive in-vivo testing, similar to previous protocols[43,44]. Testing was performed at 8- and 16-week time points under anesthesia, with animals maintained on a temperature-controlled stage at 37°C. The knee was immobilized with a clamp, and the foot was secured to a servomotor-connected footplate (Aurora Scientific, Aurora, ON, Canada). The TA was stimulated via two percutaneous 28G monopolar electrode needles (The Electrode Store, Enumclaw, WA). Stimulation amplitude was optimized by sweeping currents (4-10 mA, 1 Hz pulses), after which the optimal amplitude was applied to deliver 500 ms, 100 Hz tetanic contractions. Peak torque was calculated as the average of three independent measurements per limb, with the contralateral control serving as an internal, uninjured reference.

Gross and Histological Analysis

At designated endpoints, rats were euthanized and bilateral TA and EDL muscles harvested, weighed, and photographed. A subset of TA muscles underwent 3D scanning for volumetric analysis. TA muscles were fixed in 10% neutral-buffered formalin, bisected at the defect midline, paraffin-embedded, and sectioned. Immunolabeling was performed on deparaffinized, antigen-retrieved sections using the following primary antibodies: mouse anti-CD31 (Abcam, Waltham, MA), rabbit anti-neurofilament (Invitrogen, Waltham, MA), rabbit anti-CD68 (Bio-Rad, Hercules, CA), mouse anti-CD11b (Abcam), rabbit anti-myogenin (Abcam), and mouse anti-myosin heavy chain (MHC; DSHB, Iowa City, IA). Dual staining employed the ImmPRESS Duet Double Staining HRP/AP Kit (Vector Laboratories, Newark, CA). Single stains used the ImmPRESS-AP Polymer Kit with ImmPACT Vector Red Substrate (Vector Laboratories). Slides were counterstained with hematoxylin and scanned on an Aperio VERSA 8 whole-slide scanner (Leica Biosystems, Deer Park, IL).

3D Scanning

Excised TA muscles (16 weeks post-treatment) were cleaned of fascia and placed on a non-reflective surface for scanning with a Creaform Go!SCAN SPARK handheld 3D scanner (Houston, TX) using VXElements software (version 10.0.1.10229; Creaform, Inc.; https://www.creaform3d.com/en/products/software). Resolution was 0.8 mm, with high reflectivity and semi-rigid object settings enabled. Muscles were manually segmented, and closed volumes generated using the “Fill Holes” function with low curvature and smooth boundary (layer = 2).

Vessel Morphometric Analysis

$CD31^+$ cells and vessel structures were binarized using a neural network-based pixel classifier in Python (PyTorch, version 2.5.1; https://pytorch.org/) trained on annotated images. Binarized tile images were segmented in ImageJ (version 1.54p; https://imagej.net/software/ij/) with the “Analyze Particles” function to quantify $CD31^+$ cell/vessel density and cross-sectional area.

Spatial Transcriptomic Analysis

TA muscles treated with LD Scaffolds were harvested at 2 and 8 weeks post-treatment (n = 2-4 per time point), bisected at the defect midline, and embedded in OCT for cryosectioning. Samples were flash frozen in liquid nitrogen and stored at -80°C. Leveled cryosectioning with H&E staining was used to identify central implant regions for transcriptomics. Selected cryosections were submitted to the Indiana University School of Medicine Center for Medical Genomics for quality control, optimization, and transcriptomic analysis. RNA quality was assessed using an Agilent Bioanalyzer 2100 (Agilent Technologies, Santa Clara, CA), with RNA integrity >7.5 required for inclusion. Tissue permeabilization times were optimized using the 10X Genomics Tissue Optimization kit (10X Genomics, Pleasanton, CA). Spatial transcriptomics was performed on the 10X Visium platform following the manufacturer's protocol (CG000239, Visium Spatial Gene Expression for Fresh Frozen). The final libraries were sequenced on an Illumina NovaSeq X PLUS sequencer (Illumina, San Diego, CA). H&E staining prior to permeabilization followed the Visium platform protocol (10X Genomics).

Data Processing and Analysis

Raw sequencing data were processed with Space Ranger (version 3.1.2; 10X Genomics; https://www.10xgenomics.com/support/software/space-ranger). The sequence data were aligned to the rat reference genome mRatBN7. The filtered feature-spot matrices generated by Space Ranger were used for further analysis. Analyses were performed in R (version 4.4.2; R Foundation for Statistical Computing, Vienna, Austria; https://www.r-project.org/) using the Seurat package (version 5.1.0). SCTransform normalization was applied, and datasets were merged prior to clustering. Principle Component Analysis (PCA) was conducted, with the top 40 principal components used to identify neighbors (FindNeighbors) (k = 30). Clustering was conducted using FindClusters at a resolution of 0.5 and Uniform Manifold Approximation and Projections (UMAP) were generated using RunUMAP. Differentially expressed genes (DEGs) were identified using FindAllMarkers (min.pct = 0.1, logfc.threshold = 0.25). Gene set enrichment analysis (GSEA) was conducted with ClusterProfiler (version 4.14.4), excluding mitochondrial and ribosomal genes. Histology-based regional annotations were applied in Loupe Browser 8 (version 8.1.2; 10X Genomics; https://www.10xgenomics.com/support/software/loupe-browser) using morphology-defined regions: (1) scaffold with no cellularization or remodeling, (2) scaffold cellularization with infiltrating single cells, (3) regenerating muscle with centrally nucleated myofibers, (4) mature muscle with peripheral nuclei, and (5) fascia at the muscle border. Key genes were identified from DEGs for each region. Data visualization employed ggplot2 (version 4.0.0) and Seurat.

Spot Deconvolution using a Single Nucleus Reference Dataset

Cell type deconvolution of Visium capture spots was performed using RCTD[45], with a single-nucleus reference dataset of muscle injury and reparative healing[46]. Normalized weights were used to calculate relative cell type abundance per spot and summarized across annotated tissue regions. Visualization was performed using ggplot2 and Seurat.

Statistical Analysis

Data were analyzed in GraphPad Prism (version 6.07; GraphPad Software, Boston, MA; https://www.graphpad.com/) and presented as mean ± standard deviation. Statistical analysis used one-way analyses of variance (ANOVA) with Tukey's post hoc test. Statistical significance was set at $p<0.05$.

Results

Restoring Muscle Geometry and Preventing Void Contraction Are Key Determinants of Oligomer Scaffold-Induced Muscle Restoration

To determine how Oligomer scaffold configuration influences restoration outcomes after VML, three prototypes differing in application format and fibrillar density were tested in a rat full-thickness TA defect model (**Figure 1**). Restoration was assessed through longitudinal measures of muscle function, morphology and remodeling, with untreated defects serving as controls. Spatial transcriptomic profiling of Oligomer LD Scaffolds provided complementary insight into cellular and molecular remodeling pathways. All animals exhibited normal growth over the 16-week study period, with body weights increasing from 361 ± 16.4 g at baseline to 445 ± 48 g at 16 weeks, representing a 23% mean increase. A corresponding 12.8% increase in contralateral control TA muscle volume was observed between weeks 2 and 16, consistent with physiological muscle growth during this period.

Implantation of the HD Scaffold resulted in the greatest recovery of muscle function at both 8- and 16-weeks, with >60% increase in average torque compared to untreated controls ($p < 0.05$) and reaching ~72% of contralateral control values by 16 weeks (**Figure 2a-b**). In-Situ and LD groups exhibited moderate functional improvements, with no significant difference from either HD or untreated groups. As expected, the untreated control group consistently exhibited poor function, averaging 40-45% of contralateral control across the 16-week period.

To assess muscle mass and volume restoration, TA muscle weights were measured at 8- and 16-week time points. No significant differences were observed among groups at 8 weeks (**Figure 2c**), likely reflecting the expected lower density of Oligomer scaffolds relative to normal muscle. By 16 weeks (**Figure 2d**), the HD group exhibited the greatest muscle mass restoration (~95% of contralateral control), followed by the In-Situ group with intermediate recovery. The LD group showed modest, variable gains but was not significantly different from the untreated controls. Consistently, untreated muscles exhibited the lowest mass (~60% of the contralateral control), reflecting contracture and volume loss. Three-dimensional surface scans obtained at 16 weeks (**Supplementary Figure S2**) confirmed these trends. HD Scaffolds best restored muscle geometry (e.g., shape and size) and volume, while In-Situ and LD Scaffolds showed partial volume preservation with modest evidence of contraction and irregular muscle surface morphology. Untreated defects displayed marked volume loss and distortion.

Histological analyses of MHC-immunolabeled muscle explant cross-sections further supported these findings and revealed differences in scaffold integration and remodeling amongst the groups. In-Situ Scaffolds, which had the lowest fibrillar density, supported the most rapid integration and new muscle formation, with newly formed MHC^+ myofibers evident throughout the implant at 2 weeks (**Figure 2e**). LD Scaffolds showed intermediate levels of integration and regenerative

remodeling, consistent with their intermediate fibrillar density. In-Situ and LD Scaffolds were no longer identifiable by 16 weeks (**Figure 2f**). Notably, both groups occasionally showed evidence of implant displacement and defect cavity collapse, indicating reduced capacity to preserve defect volume under contractile forces of this VML model. Such disruptions of structural-mechanical continuity likely affected mechanochemical signaling, contributing to variability in mass, geometry, and functional outcomes.

By contrast, HD Scaffolds consistently filled the void and maintained muscle geometry throughout the study, providing mechanical stability and continuity across the injury site. As expected with their higher fibrillar density, HD Scaffolds showed the slowest rate of early cell infiltration, but by 16 weeks the majority of scaffolds were fully populated with new myofibers (**Figure 2e-f**) and displayed hierarchical histoarchitecture closely resembling native muscle (**Supplementary Figure S1a-b**). In contrast, untreated defects contracted, with scar tissue formation and disorganized muscle fiber histoarchitecture evident at 2 weeks and persisting at 16 weeks.

Taken together, these results demonstrate that early cellularization and rapid remodeling alone are insufficient for functional muscle restoration. Instead, preservation of defect geometry and prevention of void contraction are key determinants of regenerative outcomes. The HD Scaffold's physical stability enabled sustained filling and maintenance of the defect, while also fostering a controlled cellularization and remodeling response, thereby providing the structural continuity and mechanochemical cues required for regenerative healing and supporting restoration of muscle structure and function. Moreover, the progressive increase in regenerated TA muscle mass, coupled with the organization of mature myofibers, suggests that Oligomer scaffold-mediated regeneration produced muscle tissue capable of adaptive growth in concert with the host, consistent with physiological remodeling and maturation observed in healthy muscle.

Spatial Transcriptomics Reveals Spatiotemporal Signaling Pathways Underlying Oligomer Scaffold-Induced Regenerative Remodeling

Spatial transcriptomics was utilized to define the cellular and molecular mechanisms underlying Oligomer scaffold-induced regenerative remodeling. The LD Scaffold, which has an intermediate fibrillar density and a correspondingly moderate remodeling rate, was used for spatial transcriptomic analysis. Profiling was performed at 2 and 8 weeks, representing early and intermediate stages of the remodeling process. In total, ~1.38 billion sequencing reads were obtained across 13,169 spots, with a median of 1,070 genes per spot. Histological evaluation of H&E-stained spatial transcriptomics samples revealed that the LD Scaffold was visible at 2 weeks, with evidence of substantial cellular infiltration and new myofiber formation, whereas by 8 weeks the implant appeared largely remodeled.

Unsupervised Clustering and Functional Enrichment

Unsupervised clustering identified 13 distinct transcriptional clusters across all samples (**Figure 3a**). Spatial mapping revealed distinct patterns at 2 and 8 weeks, with clusters 1, 6, and 9 represented across both time points (**Figure 3b and Supplementary Figure S3a**). GSEA was conducted to further characterize the biological functions of each cluster (**Figure 3c**). Cluster 0 was excluded due to an

insufficient number of DEGs. Clusters 3, 5, 8, and 9 were enriched for early tissue remodeling pathways, including extracellular matrix organization, collagen fibril organization, and cell migration and activation. These same clusters were also enriched for vascular development, while clusters 3 and 5 specifically showed enrichment for axon development, indicating early vascularization and innervation. Pathways associated with muscle development were enriched in clusters 1, 6, and 10. Notably, clusters 1 and 6 also exhibited upregulation of neuromuscular process pathways, further supporting the role of innervation during regenerative remodeling. Mature neural markers were observed in cluster 12, and metabolic pathways were upregulated in clusters 2, 4, 6, and 7. Collectively, these results indicate that Oligomer scaffold remodeling activates spatiotemporal programs of tissue remodeling, myogenesis, and neurovascular integration that drive the re-establishment of the multicellular histoarchitecture essential for functional muscle restoration.

Regional Annotation of Tissue Regions

H&E-stained sections from transcriptomic samples were annotated into tissue regions to align transcriptional clusters with histological features (**Figure 3d**). As expected, the scaffold region showed low overall gene expression, overlapping with cluster 0, which contained few DEGs (**Supplementary Figure S3b**). The scaffold cellularization region exhibited strong upregulation of genes linked to progenitor activity (*Sox4*, *Foxp1*), ECM organization and remodeling (*Col1a1*, *Col6a1*, *Col12a1*, *Loxl2*, *Mmp14*, *Lum*), and cell migration and tissue development (*Lrrc15*, *Tnn*, *Postn*, *Tshz2*). This region corresponded primarily to cluster 3, enriched for ECM remodeling, vascularization, and neurogenesis pathways (**Supplementary Figure S3b**). The regenerating muscle region was enriched for muscle-associated genes, including regulators of myoblast activity and early myogenesis (*Mustn1*, *Dlk1*, *Myh8*, *Myl4*) and genes involved in sarcomere assembly and muscle maturation (*Actn2*, *Des*, *Sln*, *Myoz2*, *Tcap*, *Mybpc1*). Regenerating muscle regions across both 2 and 8 weeks displayed the greatest cluster diversity, reflecting heterogeneous stages of myogenesis. Consistently, GSEA revealed enrichment of vascular, myogenic, neuromuscular, and metabolic pathways in these regions (**Supplementary Figure S3b-c**). Mature muscle regions exhibited modest transcriptional activity, dominated by mitochondrial and metabolic genes (*Mt-nd4l*, *Mt-atp8*, *Pfkm*, *Gapdh*, *Ppp1r3c*) and contraction-associated genes (*Actn3*, *Tnnc2*, *Tpm1*). Likewise, these regions were primarily associated with metabolism GSEA pathways (**Supplementary Figure S3b-c**). Fascia corresponded mainly to clusters 5 and 8, enriched for ECM remodeling and immune response pathways, consistent with its in-vivo function.

Collagen Turnover and Mechanotransduction

Building on previous findings that Oligomer scaffolds promote regenerative remodeling through physiological collagen turnover and mechanotransduction cues[35,37,41], we analyzed key genes related to ECM organization, collagen dynamics, and mechanotransduction. Consistent with GSEA results (**Figure 3d**), genes associated with ECM and basement membrane structure, turnover, and organization were most strongly expressed in the scaffold cellularization region, with moderate expression in regenerating muscle at 2 weeks (**Figure 4a-b**). Specifically, fibrillar (*Col1a1*, *Col3a1*) and network-forming (*Col4a1*, *Col6a1*) collagens were upregulated. Matrix metalloproteinase (MMP; *Mmp2*, *Mmp14*) expression was detected in the scaffold cellularization region, together with modest

expression of the MMP regulator *Timp1*. This balanced expression profile reflects controlled, physiologic collagen turnover characteristic of regenerative remodeling, rather than the inflammatory-mediated degradation typically observed with conventional dECM implants[47]. Laminin (*Lamb1*) was enriched in regenerating muscle, consistent with new myofiber formation and basal lamina assembly. Mechanotransduction-associated genes showed region-specific enrichment, with *Yap1*, *Taz*, and *Piezo1* elevated in regenerating muscle and *Ctnnb1* and *Rhoa* upregulated in scaffold cellularization regions at 2 weeks. By 8 weeks, expression of MMPs, *Timp1*, and mechanotransduction genes largely resolved, indicating a transition to later-stage remodeling. Genes involved in cell-ECM and muscle-ECM adhesion and force transmission (*Fn1*, *Itgb1*, *Dag1*, *Nid1*) were also upregulated early, particularly in scaffold cellularization and regenerating muscle. In contrast, mature muscle showed minimal expression of these remodeling genes at 2 weeks and largely lacked them by 8 weeks, apart from low-level expression of structural ECM components (*Col1a1*, *Fn1*, *Dcn*). The resolution of ECM organization and mechanotransduction pathways by 8 weeks parallels the transcriptional shift toward myogenic maturation observed in global analyses, underscoring how scaffold-guided remodeling coordinates matrix turnover with the progression of muscle regeneration.

Cellular Contributors to Regenerative Remodeling

Spatial deconvolution was performed to define the cellular players driving Oligomer scaffold-guided regenerative remodeling. During early remodeling, the scaffold cellularization region contained multiple progenitor populations, including mesenchymal cells (specifically pro-regenerative fibro-adipogenic progenitors (FAPs)), endothelial stem cells, neural progenitors, and pericytes (**Figure 4c**). These populations were supported by upregulation of progenitor-associated markers such as *Foxp1* and *Nes*, as well as lineage-specific markers for FAP (*Pdgfra*), perivascular (*Pdgfrb*) and mesenchymal (*Eng, Thy1*) cells (**Figure 4a-b**). Expression of these genes was prominent at 2 weeks in both scaffold cellularization and regenerating muscle regions but largely resolved by 8 weeks, consistent with their role in early regenerative phases.

By contrast, inflammatory cells, including neutrophils, natural killer (NK) cells and T cells, showed low representation in spatial deconvolution (**Supplementary Figure S4a**). Immunostaining for macrophage markers (CD68/CD11b) confirmed only modest macrophage presence across groups, paralleling the injury-associated inflammation seen in untreated controls (**Supplementary Figure S4c**). Importantly, macrophage levels declined markedly by 8 weeks, approaching those of resident populations in native muscle (**Supplementary Figure S1c**). Likewise, expression of inflammatory (*Ccl3*) and fibrotic (*Trem2*, *Tgfb1*) markers were minimal across regions and time points (**Supplementary Figure S4b**). Thus, the regenerative remodeling mechanism, particularly within the scaffold cellularization region, appears to be dominated by the mesenchymal and progenitor cell activity with minimal contribution by inflammatory cells.

Oligomer Scaffold Remodeling Engages Cellular and Molecular Programs Consistent with Myogenesis

While progenitor populations drive the early phases of regenerative remodeling, myogenesis emerged as a subsequent and defining phase. Spatial deconvolution

revealed that satellite cells were strongly associated with regenerating muscle and, to a lesser extent, scaffold cellularization regions at 2 weeks, but declined by 8 weeks (**Figure 5a**). In contrast, myofibers were abundant in adjacent mature muscle at both time points and progressively increased in regenerating regions by 8 weeks (**Figure 5b**). This temporal pattern consisted of enrichment of the early myofiber marker *Myh3* at 2 weeks and the late-stage marker *Myh2* by 8 weeks (**Figure 5c-d**). Isolated analysis of scaffold cellularization and regenerating muscle regions (**Figure 5e-f**) further demonstrated that genes linked to satellite cells, myoblasts, and fusion predominated at 2 weeks, while late-stage markers remained elevated at 8 weeks, consistent with ongoing myofiber maturation (**Figure 5g**).

Histological immunolabeling corroborated these transcriptomic findings and highlighted differences across experimental groups. Myogenin, a marker of activated myoblasts and nascent myofibers, was evident at 2 weeks for Oligomer scaffold groups, particularly in regenerating muscle adjacent to scaffolds (**Figure 6a**). The In-Situ Scaffold displayed the highest density of myogenin$^+$ nuclei at 2 weeks, followed by LD and HD Scaffolds. By 8 weeks, the HD group retained moderate myogenin staining, whereas LD Scaffolds showed minimal staining and In-Situ Scaffolds were largely resolved. MHC immunolabeling revealed abundant small myofibers forming adjacent to and within the scaffolds for all groups at 2 weeks (**Figure 6b**). By 8 weeks, small myofibers were most prominent in the HD Scaffolds, indicating sustained myogenesis. In some cases, moderate fiber disorganization was observed, particularly with In-Situ Scaffolds, and appeared to correlate with implant displacement and void contraction; this effect was less frequent in LD and least in HD Scaffolds. In most cases, however, newly formed mature muscle exhibited hierarchical organization resembling native tissue. In contrast, untreated defects showed myogenin$^+$ nuclei at 2 weeks embedded in dense fibrotic tissue (**Figure 6a**), with no sustained myogenesis by 8 weeks and persistent myofiber disorganization throughout (**Figure 6b**). Collectively, these findings indicate Oligomer scaffolds consistently engaged in myogenic programs characterized by early satellite cell activity, nascent myofiber formation, and progressive myofiber maturation. Scaffold fibrillar density influenced the timing and organization of these processes, with HD Scaffolds supporting the most sustained and integrated myogenesis.

Regenerative Remodeling of Oligomer Scaffolds Promotes Neurovascular Integration Essential for Muscle Restoration

Given the essential role of neurovascular structures in healthy muscle and their detection in global spatial transcriptomic analyses, we next characterized vascular and neural components during regenerative remodeling. As expected, healthy muscle displayed dense capillary networks and organized neurovascular channels (**Supplementary Figure S1d**). Building on this baseline, spatial deconvolution of LD Scaffold samples revealed early participation of endothelial stem cells by 2 weeks (**Figure 4c**). Vascularization markers VEGF (*Vegfa*) and VEGFR2 (*Kdr*) were broadly expressed across scaffold cellularization and regenerating muscle regions at both 2 and 8 weeks (**Figure 7b**). Notably, *Vegfa* and *Kdr* expression were also elevated in mature muscle at 2 weeks, likely reflecting increased metabolic demand during regenerative remodeling. Endothelial cells, including the marker CD31 (*Pecam1*), were also widely expressed across regions and time points (**Figure 7a-b**), consistent with active vascularization at 2 weeks and sustained vascular

presence at 8 weeks. *Pecam1* expression was additionally enriched in the fascia region, consistent with its vascularized nature and supportive role.

Immunostaining for CD31 for all experimental groups confirmed these findings, revealing endothelial stem cells and vascular structures within and around Oligomer scaffolds at 2 weeks (**Figure 7c**). These appeared as individual endothelial cells, capillaries, and larger vessels for all Oligomer treatments. As with myogenesis, vascularization patterns differed among scaffold types. In-Situ Scaffolds showed vascular ingrowth and vessel formation throughout the scaffold, whereas LD and HD Scaffolds showed lesser vessel formation, with the depth of endothelial cell migration and vessel formation inversely related to scaffold density. In untreated controls, vascularization was limited to the scar tissue and adjacent muscle. Quantification at 2 weeks further confirmed increased vessel diameter and density within regenerating regions across all groups (**Supplementary Figure S5**), consistent with vascular remodeling. By 16 weeks, vascular architecture had stabilized, with vessel size and distribution resembling uninjured muscle. Thus, Oligomer scaffolds supported early, spatially coordinated vascular remodeling that matured into stable architecture.

Neurogenesis followed a complementary trajectory. Spatial transcriptomics detected neural progenitors as early as 2 weeks in LD Scaffold samples (**Figure 4c**), while mature neural populations were less prominent at this time (**Figure 8a**). Early innervation was supported by upregulation of the neurogenesis marker *Nes* in scaffold cellularization regions at 2 weeks and modest expression in regenerating muscle at both 2 and 8 weeks (**Figure 8b**). By 8 weeks, mature neural markers, including *Mpz*, were strongly expressed but remained spatially sparse (**Figure 8a-b**), consistent with the focal distribution of neurovascular channels in healthy muscle (**Supplementary Figure S1d**). Importantly, enrichment of *Chrna1* within regenerating muscle regions at 2 weeks was consistent with early activation of neuromuscular junction-associated transcriptional programs (**Figure 8b**). The spatial distribution of *Chrna1* closely paralleled regenerating muscle patterns described in **Figure 4**, highlighting coordinated nerve-muscle signaling during early regenerative remodeling. Immunolabeling supported these observations, showing colocalization of neural and vascular elements within scaffold cellularization and regenerating muscle regions (**Figure 8c-d**). Blood vessels and nerves developed in parallel during early scaffold remodeling and progressively organized into mature neurovascular channels as myogenesis advanced. Together, these results indicated that Oligomer scaffolds promoted coordinated vascular and neural remodeling, encompassing early vascularization, progressive neurovascular maturation, and transcriptional activation of neuromuscular junction-associated pathways, key processes that establish the integrated microenvironment for functional muscle restoration.

Discussion

Developing off-the-shelf biomaterials capable of restoring muscle geometry and functional performance represents an important goal for improving outcomes in individuals with critical muscle loss. Conventional implantable materials evaluated for VML, including dECMs, biodegradable synthetic polymers (e.g., polycaprolactone), and natural biopolymer hydrogels, remodel through immune-

mediated degradation that leads to fibrotic tissue replacement rather than regeneration of functional muscle (see [14] for review). In contrast, the Oligomer scaffolds evaluated in this study function as restorative biomaterials, re-establishing tissue continuity, integrating with host muscle, and supporting new muscle formation. Consistent with prior reports describing their non-inflammatory regenerative remodeling behavior[37,41], the present findings extend the restorative biomaterial concept to a preclinical VML model, demonstrating in-vivo restoration of muscle structure and function.

The rodent hindlimb VML model provides a widely used platform for investigating the pathophysiology of muscle injury and evaluating candidate regenerative therapies (see [7,48] for recent reviews). In this study, three Oligomer scaffold prototypes were evaluated to determine how differences in application format and fibrillar density influenced tissue response and restoration outcomes. Scaffold configurations included a flowable, in-situ scaffold-forming formulation that conformed to irregular defect geometries and pre-formed implantable scaffolds that could be trimmed and positioned within the defect. These complementary formats revealed key structure–function relationships relevant to diverse VML clinical scenarios and established design principles for next-generation restorative biomaterials.

The rat TA VML model used here produced a severe full-thickness injury (~30% volume loss) that exceeded those commonly reported (~20%)[48,49]. This defect caused greater disruption of muscle architecture and contractile capacity. Untreated control animals exhibited a ~48–82% reduction in peak isometric torque at 8 weeks that persisted through 16 weeks, whereas conventional full-thickness defect models report 27–52% functional loss over similar time frames[48,50–53]. The corresponding muscle-mass deficit (~30% at 8 weeks and ~40% at 16 weeks) also exceeded the 15–20% reduction typically observed in smaller defect models[49,53], with pronounced contracture and fibrosis confirming reparative healing[49,50]. Functional and structural outcomes in this study were normalized to contralateral limbs rather than a sham-operated control, consistent with established practice in preclinical VML studies[48,49,51,53]; however, we acknowledge that unilateral VML may induce compensatory or systemic changes in contralateral muscle, representing a limitation that may influence absolute outcome comparisons.

Substantial functional recovery was observed following Oligomer scaffold implantation. The HD Oligomer Scaffold produced a more than 60% increase in peak isometric torque by 8 weeks, achieving ~72% of contralateral control values by 16 weeks. By this time, muscle mass reached ~95% of contralateral levels, representing near-complete structural recovery. The lower-density In-Situ and LD Scaffolds supported intermediate levels of restoration, showing moderate but statistically nonsignificant gains relative to controls. These outcomes likely reflected reduced resistance to contractile forces from adjacent intact muscle, a feature of this full-thickness defect model not necessarily representative of all VML injuries. Histological analyses corroborated these findings, showing that while the lower-density scaffolds supported more rapid remodeling and new muscle formation, they lacked sufficient mechanical integrity to maintain defect geometry, resulting in variable degrees of void contraction and altered muscle morphology.

Scaffold remodeling kinetics were not independently quantified and were inferred from longitudinal histological, structural, and functional outcomes. Because scaffold fibrillar density, application format, and microstructural organization are inherently coupled in the present study, the relative contributions of fibril alignment versus density-dependent mechanical stability cannot be independently resolved. Collectively, these findings identify Oligomer scaffold fibrillar density as a critical material design parameter governing both mechanical stability and regenerative remodeling outcomes.

Previously published full-thickness rat VML studies provide a reference framework for interpreting these results. Across multiple investigations, acellular biomaterials, including dECM hydrogels, monomeric type I collagen gels, and hyaluronic acid formulations, have produced limited recovery of muscle mass or function, with outcomes often comparable to untreated controls[51–53]. These limitations have been attributed to inadequate mechanical stability, rapid material degradation, and fibrotic tissue deposition, with little evidence of new muscle formation. Even when combined with adjunctive strategies such as minced muscle autografts, cell delivery, or rehabilitation, functional recovery remains below thresholds indicative of full restoration and did not demonstrate new muscle formation across the defect[51–56].

Decellularized skeletal muscle and related dECM materials, including UBM, SIS, and dermis-derived scaffolds, have been evaluated primarily in partial-thickness VML or abdominal wall defect models in both small and large animals[57–59]. These materials typically yield modest increases in tissue bulk but limited functional recovery. Clinical experience with dECM materials used for muscle reconstruction similarly demonstrates partial volumetric restoration without full functional recovery[60–62]. Collectively, these data underscore the limitations of current dECM material strategies, where remodeling occurs via immune-mediated degradation rather than regenerative remodeling pathways.

Multi-scale insights into cellular and gene-level mechanisms of muscle repair and regeneration, derived from histologic and spatial transcriptomic analyses, provide a framework for the rational design of next-generation restorative biomaterials. Unrepaired VML defects follow a reparative trajectory dominated by inflammation and fibrosis. Early infiltration of neutrophils, NK T cells, and macrophages promotes expansion of pro-fibrotic mesenchymal-derived cells and the emergence of *Trem2*-expressing scar-associated macrophages within the defect region by 14 days[46,63]. This environment supports dense connective tissue deposition (*Col1a1*, *Aspn*) and activation of TGF-β signaling (*Tgfbi*)[63], which suppress myogenesis and perpetuate fibrosis[50,64,65].

dECM-based materials can modulate but not eliminate these fibrotic pathways, instead following a “constructive remodeling” process characterized by macrophage-driven material degradation (phagocytosis and proteolytic breakdown) and deposition of fibrovascular connective tissue rather than organized myogenesis[66–69]. In a canine partial-thickness VML model evaluated by single-nuclei and spatial transcriptomics, porcine UBM hydrogels promoted infiltration of macrophages and fibrotic mesenchymal cell populations within the defect[13].

Consistent with this paradigm, degradation (*Adam12*, *Adamts17*), connective-tissue deposition (*Col1a1*, *Col3a1*), and TGF-β pathway (*Tgfb2*, *Tgfbr2*) genes were upregulated. Spatially, fibrotic cell populations extended across the defect, while myogenic and angiogenic cells remained confined to the periphery. Thus, while dECM hydrogels may modulate inflammation observed with reparative healing and promote some myogenic activity, persistent fibrotic signaling continues to limit complete muscle restoration.

In contrast, Oligomer scaffolds induced a regenerative remodeling process characterized by early progenitor recruitment and coordinated activation of myogenic, vascular, and neural pathways (**Figure 9**). In adult muscle, regeneration depends on basal lamina-derived cues to guide satellite cell activity; however, in VML, loss of the instructive ECM framework, disruption of muscle architecture, and accompanying inflammation favor reparative fibrotic healing[7]. By filling the muscle void with an engineered fibrillar collagen scaffold that resists contraction, minimizes inflammation, and supports cellular infiltration, Oligomer scaffolds re-established the structural and mechanochemical cues required for organized myogenesis. The early establishment of a collagen-rich fibrillar matrix mirrors skeletal muscle morphogenesis, during which aligned collagen fibrils form before myotendinous junction assembly and provide a scaffold for muscle formation[70]. Similarly, Oligomer scaffold-mediated cues supported cellular migration and progenitor activity, providing the framework that guided a regenerative trajectory that parallels muscle morphogenesis despite reliance on adult progenitor sources.

Spatial transcriptomic profiling further defined a regenerative remodeling mechanism for Oligomer scaffolds that contrasted the responses observed in unrepaired and dECM-treated defects. Unlike conventional collagen materials that undergo macrophage-driven degradation[47], Oligomer scaffolds were immunotolerant, avoiding foreign-body reactions and immune-mediated degradation[41]. At 2 weeks, immune cell presence was minimal, and macrophage populations lacked pro-inflammatory (*Ccl3*) and scar-associated (*Trem2*) signatures, consistent with a restorative trajectory distinct from reparative healing and constructive remodeling. Macrophages were diffusely distributed rather than clustered, and largely resolved by 8 weeks, consistent with a transient, injury-associated immune response. In the absence of sustained inflammation, TGF-β (*Tgfb1*) expression remained modest and spatially dispersed.

In place of fibrotic cell populations, Oligomer-treated regions displayed enrichment of pericytes, endothelial and neural progenitors, satellite cells, and pro-regenerative mesenchymal cells. These multi-lineage populations defined a regenerative cellular niche distinct from the pro-fibrotic environments of untreated or dECM-treated defects[13,63]. Consistent with this cellular response, gene-level analyses revealed enrichment of laminin, proteoglycans, and basement-membrane ECM proteins within scaffold cellularization zones, contrasting with the collagen I–dominant profiles (*Col1a1*, *Col3a1*) typical of fibrosis. Regenerating regions also expressed

early (*Myod1*, *Myh3*) and mature (*Acta1*, *Myh2*) myogenic markers, confirming active muscle formation throughout the defect.

The regenerative response supported by Oligomer scaffolds recapitulated key aspects of developmental myogenesis. During embryonic muscle formation, myogenic progenitors migrate into the limb bud and differentiate under canonical myogenic regulators (*Myod1*, *Myog*)[71,72], while angiogenic and neural programs mature concurrently[73–76]. Similarly, Oligomer scaffolds elicited a temporally organized myogenic response, with early-stage markers (*Myod1*, *Myog*, *Myh3*) enriched at 2 weeks and mature contractile genes elevated by 8 weeks (*Myh2*, *Myh4*, *Acta1*). Parallel upregulation of angiogenic (*Vegfa*, *Kdr*) and neuromuscular junction–associated (*Chrna1*) genes, along with histological evidence of organized neurovascular networks, confirmed coordinated multi-lineage regeneration. By re-establishing mechanical continuity and synchronizing activation of myogenic, vascular, and neural activity, Oligomer scaffolds guided regenerative healing along a developmental-like trajectory that promoted restoration of muscle structure and function. The progressive increase in regenerated muscle mass, in concert with host growth, further supported physiological integration and adaptive capacity characteristic of mature skeletal muscle.

Collectively, these results demonstrate that Oligomer scaffolds support a distinct, immunotolerant regenerative remodeling process that restores muscle architecture and function while avoiding the fibrotic pathways characteristic of reparative or constructive remodeling. Scaffold fibrillar microstructure and mechanical integrity emerged as key determinants of restoration outcomes, enabling re-establishment of native muscle geometry while supporting new muscle formation. The complementary attributes of the pre-formed implantable and flowable in-situ scaffold-forming formulations suggest a versatile design platform capable of addressing diverse geometries and clinical contexts of muscle injury. Notably, the in-situ scaffold-forming formulation has received FDA 510(k) clearance (Product Code KGN) for use in wound management, underscoring its regulatory maturity and potential adaptability to other surgical indications such as VML. Building on these full-thickness defect findings, future studies in other clinically relevant injury contexts and large animal models will be important to further define performance and translational potential. Overall, this work establishes the mechanistic foundation for Oligomer scaffold-mediated muscle regenerative remodeling and provides a framework for continued development of restorative biomaterials that re-establish muscle structure and function through non-inflammatory, integrative remodeling.

Acknowledgements

The authors would like to thank the members of the Weldon School of Biomedical Engineering Preclinical Studies Team, including G. Brock, L. Carrell, and M. Bible. For histological analysis, we would like to acknowledge the assistance of the Purdue University Histology Research Laboratory, a core facility of the NIH-funded Indiana Clinical and Translational Science Institute. For transcriptomic analysis, we would

like to thank the Center for Medical Genomics at the Indiana University School of Medicine, which is partially supported by the Indiana University Grand Challenges Precision Health Initiative.

Funding
This research was funded by generous donations from the McKinley Family Foundation.

Author Contributions

R.A.M., J.S., L.Z., and S.V.-H. generated the concept and designed the study. R.A.M., J.S., L.Z., and E.D. conducted the experimental procedures. S.V.-H., R.A.M., J.S., E.D., and M.P. analyzed the data. H.G. and Y.L. assisted with the acquisition and interpretation of transcriptomic data. S.V.-H., S.H., and T.H.Q. provided project guidance and feedback. S.V.-H., R.A.M., J.S., and E.D. contributed to manuscript drafting, and all authors reviewed, provided comments, and edited the manuscript.

Data Availability

The spatial transcriptomics datasets generated in this study have been deposited in the National Center for Biotechnology Information (NCBI) Gene Expression Omnibus (GEO) under accession number GSE310073. All other data generated or analyzed in this study are available from the corresponding author upon reasonable request.

Additional Information

Competing Interests: S.V.-H. is the founder and a shareholder of GeniPhys, Inc. S.V.-H. does not hold an executive or operational role with the company. All other authors declare no competing interests.

Supplementary Information

Supplementary information is included in the dedicated Supplementary Information files.

References

1. Chi, D. *et al.* Free functional muscle transfer for lower extremity reconstruction. *J. Plast. Reconstr. Aesthet. Surg.* **86**, 288–299 (2023).
2. Zhang, Q. *et al.* Harnessing the synergy of perfusable muscle flap matrix and adipose-derived stem cells for prevascularization and macrophage polarization to reconstruct volumetric muscle loss. *Bioact. Mater.* **22**, 588–614 (2023).
3. Zhao, G. *et al.* Local muscle or myocutaneous flap transfer for emergent repair of Gustilo IIIB open tibiofibular fractures. *Sci. Rep.* **14**, 25609 (2024).
4. Griepp, D. W. *et al.* Outcomes of gracilis free-flap muscle transfers and non-free-flap procedures for restoration of elbow flexion: A systematic review. *J. Plast. Reconstr. Aesthet. Surg.* **75**, 2625–2636 (2022).
5. Langridge, B., Griffin, M. & Butler, P. E. Regenerative medicine for skeletal muscle loss: A review of current tissue engineering approaches. *J. Mater. Sci. Mater. Med.* **32**, 15 (2021).
6. Gahlawat, S. *et al.* Tissue engineered 3D constructs for volumetric muscle loss. *Ann. Biomed. Eng.* **52**, 2325–2347 (2024).
7. Greising, S. M., Corona, B. T., McGann, C., Frankum, J. K. & Warren, G. L. Therapeutic approaches for volumetric muscle loss injury: A systematic review and meta-analysis. *Tissue Eng. Part B Rev.* **25**, 510–525 (2019).
8. Rose, L. F. *et al.* The convergence of regenerative medicine and rehabilitation: Federal perspectives. *NPJ Regen. Med.* **3**, 19 (2018).
9. Zhang, C. & Gao, Y. The role of transmembrane proteins on force transmission in skeletal muscle. *J. Biomech.* **47**, 3232–3236 (2014).
10. Mukund, K. & Subramaniam, S. Skeletal muscle: A review of molecular structure and function, in health and disease. *Wiley Interdiscip. Rev. Syst. Biol. Med.* **12**, e1462 (2019).
11. Sousa-Victor, P., García-Prat, L. & Muñoz-Cánoves, P. Control of satellite cell function in muscle regeneration and its disruption in ageing. *Nat. Rev. Mol. Cell Biol.* **23**, 204–226 (2022).
12. Kaczmarek, A. *et al.* The role of satellite cells in skeletal muscle regeneration—The effect of exercise and age. *Biology (Basel)* **10**, 1056 (2021).
13. Giannone, A. A. *et al.* Deconstruction of cellular dynamics after treatment of volumetric muscle loss injury with extracellular matrix. *NPJ Regen. Med.* **10**, 45 (2025).
14. Carnes, M. E. & Pins, G. D. Skeletal muscle tissue engineering: Biomaterials-based strategies for the treatment of volumetric muscle loss. *Bioengineering (Basel)* **7**, 85 (2020).
15. Smoak, M. M. & Mikos, A. G. Advances in biomaterials for skeletal muscle engineering and obstacles still to overcome. *Mater. Today Bio.* **7**, 100069 (2020).

16. Schiltz, L., Grivetti, E., Tanner, G. I. & Qazi, T. H. Recent advances in implantable biomaterials for the treatment of volumetric muscle loss. *Cells Tissues Organs.* **213**, 486–502 (2024).
17. Wang, Z., Liang, W., Ao, R. & An, Y. Adipose decellularized matrix: A promising skeletal muscle tissue engineering material for volume muscle loss. *Biomater. Res.* **29**, 0174 (2025).
18. Urciuolo, A. *et al.* Decellularised skeletal muscles allow functional muscle regeneration by promoting host cell migration. *Sci. Rep.* **8**, 8398 (2018).
19. Yu, W. *et al.* Bioactive nanofiber-hydrogel composite regulates regenerative microenvironment for skeletal muscle regeneration after volumetric muscle loss. *Adv. Healthc. Mater.* **13**, e2304087 (2024).
20. Pollot, B. E., Rathbone, C. R., Wenke, J. C. & Guda, T. Natural polymeric hydrogel evaluation for skeletal muscle tissue engineering. *J. Biomed. Mater. Res. B Appl. Biomater.* **106**, 672–679 (2018).
21. Kim, J. H. *et al.* 3D bioprinted human skeletal muscle constructs for muscle function restoration. *Sci. Rep.* **8**, 12307 (2018).
22. Das, S. *et al.* Pre-innervated tissue-engineered muscle promotes a pro-regenerative microenvironment following volumetric muscle loss. *Commun. Biol.* **3**, 330 (2020).
23. Quarta, M. *et al.* Bioengineered constructs combined with exercise enhance stem cell-mediated treatment of volumetric muscle loss. *Nat. Commun.* **8**, 15613 (2017).
24. McKellar, D. W. *et al.* Large-scale integration of single-cell transcriptomic data captures transitional progenitor states in mouse skeletal muscle regeneration. *Commun. Biol.* **4**, 1280 (2021).
25. Ruta, A., Krishnan, K. & Elisseeff, J. H. Single-cell transcriptomics in tissue engineering and regenerative medicine. *Nature Reviews Bioengineering* **2**, 101–119 (2024).
26. Oprescu, S. N., Yue, F., Qiu, J., Brito, L. F. & Kuang, S. Temporal dynamics and heterogeneity of cell populations during skeletal muscle regeneration. *iScience* **23**, 100993 (2020).
27. Castor-Macias, J. A. *et al.* Reprogramming of myeloid responses to volumetric muscle loss via engineered protein nanoparticles. *ACS Nano* **19**, 30441–30454 (2025).
28. Kreger, S. T. *et al.* Polymerization and matrix physical properties as important design considerations for soluble collagen formulations. *Biopolymers* **93**, 690–707 (2010).
29. Bailey, J. L. *et al.* Collagen oligomers modulate physical and biological properties of three-dimensional self-assembled matrices. *Biopolymers* **95**, 77–93 (2011).
30. Blum, K. M. *et al.* Acellular and cellular high-density, collagen-fibril constructs with suprafibrillar organization. *Biomater. Sci.* **4**, 711–723 (2016).
31. Novak, T. *et al.* Mechanisms and microenvironment investigation of cellularized high density gradient collagen matrices via densification. *Adv. Funct. Mater.* **26**, 2617–2628 (2016).
32. Buno, K. P. *et al.* In vitro multitissue interface model supports rapid vasculogenesis and mechanistic study of vascularization across tissue compartments. *ACS Appl. Mater. Interfaces* **8**, 21848–21860 (2016).

33. Whittington, C. F., Yoder, M. C. & Voytik-harbin, S. L. Collagen-polymer guidance of vessel network formation and stabilization by endothelial colony forming cells in vitro. *Macromol. Biosci.* **13**, 1135–1149 (2013).
34. Brookes, S., Voytik-Harbin, S., Zhang, H. & Halum, S. Three-dimensional tissue-engineered skeletal muscle for laryngeal reconstruction. *Laryngoscope* **128**, 603–609 (2018).
35. Sohutskay, D. O., Buno, K. P., Tholpady, S. S., Nier, S. J. & Voytik-Harbin, S. L. Design and biofabrication of dermal regeneration scaffolds: Role of oligomeric collagen fibril density and architecture. *Regen. Med.* **15**, 1295–1312 (2020).
36. Shay, E. O. *et al.* Scaffold-forming collagen and motor-endplate expressing muscle cells for porcine laryngoplasty. *Laryngoscope* **134**, 4988–4997 (2024).
37. Puls, T. J. *et al.* Regenerative tissue filler for breast conserving surgery and other soft tissue restoration and reconstruction needs. *Sci. Rep.* **11**, 2711 (2021).
38. Brookes, S. *et al.* Laryngeal reconstruction using tissue-engineered implants in pigs: A pilot study. *Laryngoscope* **131**, 2277–2284 (2021).
39. Wesson, T. *et al.* Multi-layered implant approach for hemilaryngectomy reconstruction in a porcine model. *Laryngoscope* **135**, 769–778 (2025).
40. Wesson, T. *et al.* Tissue-engineered implant for hemilaryngectomy reconstruction with recurrent laryngeal nerve injury. *Laryngoscope* **134**, 4604–4613 (2024).
41. Morrison, R. A. *et al.* Engineered collagen polymeric materials create noninflammatory regenerative microenvironments that avoid classical foreign body responses. *Biomater. Sci.* **11**, 3278–3296 (2023).
42. Voytik-Harbin, S. L., Novak, T. A., Blum, K. & Neu, C. P. Collagen compositions and methods of use. United States Patent US11478574B2 (2022).
43. Mintz, E. L., Passipieri, J. A., Lovell, D. Y. & Christ, G. J. Applications of in vivo functional testing of the rat tibialis anterior for evaluating tissue engineered skeletal muscle repair. *J. Vis. Exp.* **7**, e54487 (2016).
44. Gerlinger-Romero, F. *et al.* Non-invasive assessment of dorsiflexor muscle function in mice. *J. Vis. Exp.* **143**, e58696 (2019).
45. Cable, D. M. *et al.* Robust decomposition of cell type mixtures in spatial transcriptomics. *Nat. Biotechnol.* **40**, 517–526 (2022).
46. Larouche, J. A. *et al.* Neutrophil and natural killer cell imbalances prevent muscle stem cell-mediated regeneration following murine volumetric muscle loss. *Proc. Natl. Acad. Sci. U. S. A.* **119**, e2111445119 (2022).
47. Valentin, J. E., Stewart-Akers, A. M., Gilbert, T. W. & Badylak, S. F. Macrophage participation in the degradation and remodeling of extracellular matrix scaffolds. *Tissue Eng. Part A* **15**, 1687–1694 (2009).
48. Dolan, C. P., Dearth, C. L., Corona, B. T. & Goldman, S. M. Retrospective characterization of a rat model of volumetric muscle loss. *BMC Musculoskelet. Disord.* **23**, 814 (2022).
49. Garg, K., Corona, B. T. & Walters, T. J. Losartan administration reduces fibrosis but hinders functional recovery after volumetric muscle loss injury. *J. Appl. Physiol. (1985)* **117**, 1120–1131 (2014).
50. Aguilar, C. A. *et al.* Multiscale analysis of a regenerative therapy for treatment of volumetric muscle loss injury. *Cell Death Discov.* **4**, 33 (2018).
51. Ward, C. L., Ji, L. & Corona, B. T. An autologous muscle tissue expansion approach for the treatment of volumetric muscle loss. *Biores. Open Access* **4**, 198–208 (2015).

52. Goldman, S. M. & Corona, B. T. Co-delivery of micronized urinary bladder matrix damps regenerative capacity of minced muscle grafts in the treatment of volumetric muscle loss injuries. *PLoS One* **12**, e0186593 (2017).
53. Goldman, S. M., Henderson, B. E. P., Walters, T. J. & Corona, B. T. Co-delivery of a laminin-111 supplemented hyaluronic acid based hydrogel with minced muscle graft in the treatment of volumetric muscle loss injury. *PLoS One* **13**, e0191245 (2018).
54. Garg, K., Ward, C. L., Rathbone, C. R. & Corona, B. T. Transplantation of devitalized muscle scaffolds is insufficient for appreciable de novo muscle fiber regeneration after volumetric muscle loss injury. *Cell Tissue Res.* **358**, 857–873 (2014).
55. Corona, B. T. *et al.* Autologous minced muscle grafts: A tissue engineering therapy for the volumetric loss of skeletal muscle. *Am. J. Physiol. Cell Physiol.* **305**, C761-75 (2013).
56. Aurora, A., Roe, J. L., Corona, B. T. & Walters, T. J. An acellular biologic scaffold does not regenerate appreciable de novo muscle tissue in rat models of volumetric muscle loss injury. *Biomaterials* **67**, 393–407 (2015).
57. Ma, J., Sahoo, S., Baker, A. R. & Derwin, K. A. Investigating muscle regeneration with a dermis/small intestinal submucosa scaffold in a rat full-thickness abdominal wall defect model. *J. Biomed. Mater. Res. B Appl. Biomater.* **103**, 355–364 (2015).
58. Corona, B. T. & Greising, S. M. Challenges to acellular biological scaffold mediated skeletal muscle tissue regeneration. *Biomaterials* **104**, 238–246 (2016).
59. Valentin, J. E., Turner, N. J., Gilbert, T. W. & Badylak, S. F. Functional skeletal muscle formation with a biologic scaffold. *Biomaterials* **31**, 7475–7484 (2010).
60. Sicari, B. M. *et al.* An acellular biologic scaffold promotes skeletal muscle formation in mice and humans with volumetric muscle loss. *Sci. Transl. Med.* **6**, 234ra58 (2014).
61. Mase, V. J. *et al.* Clinical application of an acellular biologic scaffold for surgical repair of a large, traumatic quadriceps femoris muscle defect. *Orthopedics* **33**, 511 (2010).
62. Dziki, J. *et al.* An acellular biologic scaffold treatment for volumetric muscle loss: Results of a 13-patient cohort study. *NPJ Regen. Med.* **1**, 16008 (2016).
63. Larouche, J. A., Wallace, E. C., Spence, B. D., Buras, E. & Aguilar, C. A. Spatiotemporal mapping of immune and stem cell dysregulation after volumetric muscle loss. *JCI Insight* **8**, e162835 (2023).
64. Girardi, F. *et al.* TGFβ signaling curbs cell fusion and muscle regeneration. *Nat. Commun.* **12**, 1–16 (2021).
65. Aurora, A., Garg, K., Corona, B. T. & Walters, T. J. Physical rehabilitation improves muscle function following volumetric muscle loss injury. *BMC Sports Sci. Med. Rehabil.* **6**, 41 (2014).
66. Badylak, S. F. The extracellular matrix as a biologic scaffold material. *Biomaterials* **28**, 3587–3593 (2007).
67. Badylak, S. F., Dziki, J. L., Sicari, B. M., Ambrosio, F. & Boninger, M. L. Mechanisms by which acellular biologic scaffolds promote functional skeletal muscle restoration. *Biomaterials* **103**, 128–136 (2016).
68. Greising, S. M. *et al.* Unwavering pathobiology of volumetric muscle loss injury. *Sci. Rep.* **7**, 1–14 (2017).

69. Badylak, S. F. Decellularized allogeneic and xenogeneic tissue as a bioscaffold for regenerative medicine: Factors that influence the host response. *Ann. Biomed. Eng.* **42**, 1517–1527 (2014).
70. Leng, Y. *et al.* Extracellular matrix deposition precedes muscle-tendon integration during murine forelimb morphogenesis. *Commun. Biol.* **8**, 1202 (2025).
71. Chal, J. & Pourquié, O. Making muscle: Skeletal myogenesis in vivo and in vitro. *Development* **144**, 2104–2122 (2017).
72. Buckingham, M. *et al.* The formation of skeletal muscle: From somite to limb. *J. Anat.* **202**, 59–68 (2003).
73. Lin, W. *et al.* Distinct roles of nerve and muscle in postsynaptic differentiation of the neuromuscular synapse. *Nature* **410**, 1057–1064 (2001).
74. Liu, W. & Chakkalakal, J. V. The composition, development, and regeneration of neuromuscular junctions. *Curr. Top. Dev. Biol.* **126**, 99–124 (2018).
75. Mayeuf-Louchart, A. *et al.* Notch regulation of myogenic versus endothelial fates of cells that migrate from the somite to the limb. *Proc. Natl. Acad. Sci. U. S. A.* **111**, 8844–8849 (2014).
76. Pepe, G. J. & Albrecht, E. D. Microvascular skeletal-muscle crosstalk in health and disease. *Int. J. Mol. Sci.* **24**, 10425 (2023).

Figure Legends

Figure 1. Experimental design for evaluation of Oligomer scaffolds in a rat VML model. Schematic of the rat TA VML injury model showing creation of a full-thickness defect (~30% of muscle volume). Representative intraoperative images illustrate defect creation and treatment with one of three Oligomer scaffold prototypes: In-Situ self-assembling scaffold, Low Density (LD) preformed scaffold, or High Density (HD) preformed scaffold. Untreated defects served as controls. The experimental timeline summarizes groups and endpoints for functional testing, gross morphology, histology, immunolabeling, and spatial transcriptomic analysis. Asterisk indicates that spatial transcriptomic analyses were performed for the LD Scaffold treatment.

Figure 2. In-vivo muscle function, muscle weight, and histological assessment of Oligomer-treated and untreated VML defects. (a,b) Peak isometric torque of the TA muscle and **(c,d)** TA muscle explant weights at **(a,c)** 8 weeks and **(b,d)** 16 weeks post-surgery across treatment groups: In-Situ (IS),

LD, and HD Oligomer scaffolds, and no treatment (NT) controls. The dashed line represents the average value of the contralateral (uninjured) control muscle. Different letters indicate statistically significant differences between groups ($p<0.05$); groups sharing same letter are not statistically different. **(e-f)** Representative transverse sections of muscle explants at **(e)** 2 weeks and **(f)** 16 weeks post-treatment, immunolabeled for MHC (red) to assess muscle regeneration and organization. Asterisks denote Oligomer scaffolds, and arrow highlights scar tissue at 2 weeks. Scale bars = 2 mm.

Figure 3. Spatial and transcriptional characterization of the regenerative remodeling response in a rat VML defect treated with LD Scaffold. (a) UMAP plot displaying clustering of spatial transcriptomic profiles from LD Scaffold-treated muscle at 2 and 8 weeks post-implantation. **(b)** Representative spatial overlays depicting the localization of transcriptionally distinct clusters across regenerating muscle tissue sections. **(c)** Heatmap of normalized enrichment scores (NES) from GSEA, highlighting key regenerative pathways associated with each cluster. **(d)** Spatial annotations of tissue regions based on morphological and structural features observed across the explant section.

Figure 4. Spatial transcriptomic analysis of LD Scaffold defines early regenerative remodeling response characterized by mechanochemical signaling and pro-regenerative cell populations. (a) Spatial annotations of scaffold cellularization, regenerating muscle, and mature muscle regions 2 or 8 weeks after LD Scaffold treatment, highlighting regions discussed in violin plots. **(b)** Violin plots showing expression of marker genes associated with ECM and basement membrane organization and turnover, mechanotransduction, cell adhesion and force transmission, and progenitor and mesenchymal cells. **(c)** Spatial deconvolution overlays showing the location of mesenchymal (FAP) cells, pericytes, endothelial stem cells, and neural progenitors.

Figure 5. Spatial and transcriptional profiling reveals muscle progenitor populations and stage-specific myogenic gene expression consistent with scaffold-mediated regeneration. (a–b) Spatial deconvolution maps showing the distribution of **(a)** satellite cells and **(b)** mature myofibers at 2 and 8 weeks post-implantation of LD Scaffolds, highlighting regions of active regeneration and fiber maturation. **(c–d)** Spatial gene expression overlays for **(c)** *Myh3* (early-stage myofiber marker) and **(d)** *Myh2* (late-stage myofiber marker), demonstrating region-specific expression patterns reflective of myofiber development and maturation over time. **(e–f)** Spatial maps highlighting (red) scaffold cellularization and regenerating muscle regions selected for targeted transcriptomic analysis at **(e)** 2 weeks and **(f)** 8 weeks. **(g)** Violin plots display expression of genes associated with successive stages of myogenesis, including satellite cell activation and differentiation (*Cdh15, Myod1, Cdkn1c, Igfbp5, Myog, Mymk*), as well as early- (*Myh3, Acta1*) and late-stage (*Ckm, Myh2, Myh4*) markers of myofiber development. Expression trends over time support engagement of a regenerative myogenic program within scaffold-infiltrated and regenerating muscle regions.

Figure 6. Scaffold-dependent differences in temporal myogenic remodeling revealed by myogenin and MHC immunolabeling. (a-b)

Representative immunolabelled transverse sections at 2 and 8 weeks post-implantation showing **(a)** myogenin$^+$ nuclei (red) and **(b)** MHC$^+$ myofibers (red), illustrating scaffold-dependent differences in density and distribution of differentiating myogenic cells within regenerating muscle regions. Notably, scaffold-treated groups support progressive restoration of organized, hierarchical muscle fiber architecture, whereas the untreated group exhibits disorganized muscle architecture consistent with contracture and fibrotic scar formation. Asterisks denote Oligomer scaffold, and arrows denote myogenin$^+$ nuclei at 8 weeks. Scale bars: a = 50 µm; b = 100 µm.

Figure 7. Vascularization occurs within scaffold cellularization and regenerating muscle regions as a key aspect of regenerative remodeling. **(a)** Spatial deconvolution plots showing the distribution of endothelial cell populations and **(b)** spatial gene expression maps highlighting localized expression of vascular-associated factors *Vegf* (vascular endothelial growth factor; pro-angiogenic signaling molecule), *Kdr* (kinase insert domain receptor; VEGFR2), and *Pecam1* (platelet endothelial cell adhesion molecule-1; endothelial junction marker) at 2- and 8-weeks following implantation of LD Scaffold. **(c)** Transverse muscle sections 2 weeks after implantation of In-Situ, LD, and HD Scaffolds, compared to no treatment control, immunolabeled for CD31 (brown) and neurofilament (red) staining to identify endothelial and neural cells. Insets highlight CD31$^+$ progenitors and vascular structures (black arrows). Scale bars: 100 µm; inset = 25 µm.

Figure 8. Neurovascular complexes and neuromuscular junctions form within scaffold cellularization and regenerating muscle regions during scaffold-mediated regenerative remodeling. (a) Spatial deconvolution plots showing the distribution of neural cell populations across muscle explants at 2 and 8 weeks following implantation of the LD Scaffold. **(b)** Spatial gene expression maps highlighting localized expression of *Chrna1* (cholinergic receptor nicotinic alpha 1 subunit; neuromuscular junction-associated), *Nes* (nestin*;* neurovascular progenitor marker), and *Mpz* (myelin protein zero; Schwann cell marker), indicating the formation of neurovascular and neuromuscular structures. **(c-d)** Representative transverse sections from scaffold-treated groups across time points, immunolabelled for neurofilament (red) and CD31 (brown, endothelial marker), show neurovascular complexes in **(c)** scaffold cellularization regions and **(d)** adjacent regenerating muscle. Low-magnification images (top panels) and corresponding high-magnification views of boxed areas (bottom panels) illustrate detailed neurovascular architecture in both regions. Scale bars: top panels = 100 µm; bottom panels = 25 µm.

Figure 9. Schematic illustrating regenerative remodeling of restorative Oligomer scaffolds following VML injury. The noninflammatory regenerative remodeling process supports infiltration, organization, and integration of diverse progenitor cell populations, leading to coordinated vascularization, myogenesis, and neurogenesis.

Experimental Groups:

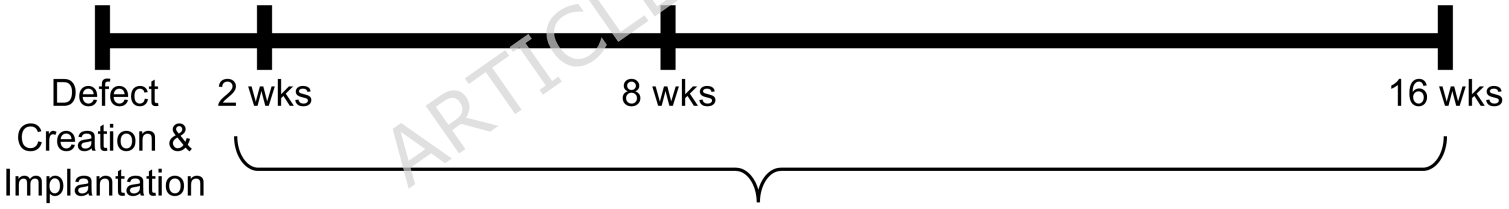

Outcomes:

- Muscle Weight (8, 16 wks)
- Muscle Function (8, 16 wks)
- Histology (2, 8, 16 wks)
- Spatial Transcriptomics* (2, 8 wks)